Nature Communications

https://doi.org/10.1038/s41467-026-69908-w

Article in Press

Drift-free ferroelectric photodetection with fast temporal response via thermal diffusion engineering

Received: 22 August 2025

Accepted: 12 February 2026

Cite this article as: Minhas, J.Z., Qian, W., Xu, L. *et al.* Drift-free ferroelectric photodetection with fast temporal response via thermal diffusion engineering. *Nat Commun* (2026). https://doi.org/10.1038/s41467-026-69908-w

Jabir Zamir Minhas, Weiqi Qian, Lan Xu, Chong Guo, Chris R. Bowen & Ya Yang

Drift-free ferroelectric photodetection with fast temporal response via thermal diffusion engineering

Jabir Zamir Minhas[1,2,†], Weiqi Qian[1,2,†], Lan Xu[1,†], Chong Guo[1,2,†], Chris R. Bowen[3] & Ya Yang[1,2*]

[1]Beijing Key Laboratory of High-Entropy Energy Materials and Devices, Beijing Institute of Nanoenergy and Nanosystems, Chinese Academy of Sciences, Beijing 101400, P.R. China.

[2]School of Nanoscience and Engineering, University of Chinese Academy of Sciences, Beijing 100049, P.R. China.

[3]Department of Mechanical Engineering, University of Bath, BA27AK, UK.

[†] These authors contributed equally: Jabir Zamir Minhas, Weiqi Qian, Lan Xu and Chong Guo.

*Correspondence to: yayang@binn.cas.cn (Tel: +86 10 60688552)

Abstract: Self-powered ferroelectric photodetectors offer an attractive platform for low-power optoelectronics, exploiting intrinsic bulk photovoltaic effects to achieve bias-free operation. However, their practical deployment has been hindered by slow temporal response and photocurrent drift, mainly due to inefficient thermal dissipation that leads to temperature buildup within the device under continuous illumination. Here, we report a thermal-diffusion-engineering approach that reconfigures the thermal environment of ferroelectric device to suppress lateral heat dissipation and enable efficient vertical heat extraction. Compared to conventional architecture, the engineered drift-free device exhibits a photoresponse speed improvement of over three orders of magnitude, along with complete drift suppression, enabling high-fidelity imaging with minimal crosstalk. Infrared thermography and COMSOL simulations confirm distinct thermal environment in conventional and drift-free devices, revealing strong heat accumulation in conventional and efficient heat extraction in drift-free architectures. This work highlights thermal diffusion engineering as a key device-design parameter for enhancing ferroelectric optoelectronic performance, paving the way for scalable, bias-free energy-harvesting photodetectors and neuromorphic imaging systems.

Keywords:

Ferroelectrics, self-powered photodetection, optoelectronics, drift-free signal, thermal diffusion.

The rapid advancement of optoelectronics has driven interest in next-generation photodetectors[1-5] featuring high sensitivity, broad spectral response, and long-term stability[6-10]. Ferroelectric (FE) thin films have emerged as particularly attractive candidates because they can (i) generate a photovoltaic (PV) response without complex p-n junctions, (ii) produce a photovoltage that exceeds the bandgap, and (iii) enable a tunable output through mechanical, electrical, or magnetic control[11-14]. This inherent coupling allows for tailored properties that enhance photovoltaic applications.

Among the range of potential FE materials, $BiFeO_3$ (BFO) is specially compelling owing to its narrow bandgap (~2.7 eV), visible-light absorption, strong remnant polarization, intrinsic multiferroicity, and stable optoelectronic performance[15-22]. These features collectively enable efficient carrier separation when illuminated due to its internal depolarization fields, thus supporting self-powered operation across the visible to near-ultraviolet spectrum The intrinsic room-temperature ferroelectricity of BFO renders it highly suitable for practical optoelectronic applications, including wearable imaging, optical communication, and neuromorphic computing[23-25].

Despite these advantages, the practical deployment of FE-based photodetectors has been hindered by persistent limitations, most notably a slow temporal response and photocurrent drift—defined as a gradual, unintended time-dependent variation in photocurrent when subject to continuous illumination. These limitations originate from illumination-induced heating and insufficient heat dissipation within the device. When the thermal environment is not well controlled, accumulated heat broadens the temporal response, reduces carrier extraction efficiency and destabilizes the steady state output. These thermally driven effects have been widely observed in oxide-based photodetectors[26-29], emphasizing that local heat distribution, is a critical but often overlooked determinant of device stability and dynamic performance.

Conventional FE photodetectors is commonly fabricated on low-thermal-conductivity substrates, such as mica or glass, with mica offering an atomically flat, chemically inert, and electrically insulating surface that is well suited for high-quality growth of perovskite oxide films[30,31]. It also withstands high-temperature processing and provides mechanical flexibility, which has made it a standard platform for many BFO and related FE devices. However, its intrinsically low thermal conductivity leads to significant lateral heat accumulation during

illumination, contributing to slow response and drift, and motivating our thermal-diffusion engineering strategy using high-k metallic backers. This phenomenon is conceptually related to thermal modulation transfer function (MTF) in pyroelectric imaging system[32], where lateral heat diffusion reduces the modulation depth and contrast of spatial signals. To improve the PV effect and overcome the associated challenges, recent strategies have focused on structural and electronic modifications[33-35]. However, microscale thermal diffusion engineering remains an unexplored, but potentially transformative, approach for improving the dynamic performance of FE photodetectors.

Here we present a thermal diffusion engineering strategy that enables drift-free operation and fast temporal response in ferroelectric photodetectors by directing vertical heat extraction through a high conductivity copper substrate. Using BFO-based films as a model system, we demonstrate that thermal confinement suppresses lateral heat diffusion, thereby maintaining stable thermal environment under continuous illumination of light. Our optimized architecture demonstrates >3 orders of magnitude faster response speed and near-complete elimination of photocurrent drift compared to conventional devices. Infrared thermal imaging and COMSOL Multiphysics simulations confirm that the thermally conductive copper substrate is able to suppress lateral heat spreading and enhancing carrier mobility. Beyond fundamental performance gains, this thermally stabilized architecture also enables high-fidelity imaging with minimal crosstalk, positioning drift-free-FE devices as promising candidates for neuromorphic vision, wearable sensing, and next-generation optoelectronic systems requiring stable, precision operation.

Results

Design of drift-free ferroelectric photodetector

A detailed comparison between conventional and drift-free photodetectors highlights (Fig. 1a-d) how the thermal transport dynamics directly influence device performance and reveal distinct operational regimes. The conventional device structure consists of lanthanum nickelate ($LaNiO_3$, LNO)/bismuth ferrite ($BiFeO_3$, BFO)/indium tin oxide (ITO) on a mica substrate (Fig. 1a), consistent with previously reported FE photodetectors[38]. The output signal characteristics reveal two fundamental limitations: a slow response time (red dotted rectangle) and notable photocurrent

drift (red curved arrow). The schematic in Fig. 1b elucidates the physical origin of these limitations: lateral thermal diffusion leads to in-plane heat spreading (circular isotherms) and causes thermal accumulation within the BFO layer which broadens the temporal response, producing the characteristic slow extraction and thermal drift.

The transformative improvement is achieved through our thermal engineering approach (Fig. 1c), where a high-thermal-conductivity copper layer is introduced beneath the mica substrate. This architecture yields a step-change in performance, eliminating photocurrent drift (blue arrow) and sharply reducing the response time (blue dotted rectangle). Vertical heat dissipation confines the local thermal gradients near the illumination site (Fig. 1d), suppresses lateral thermal spreading and maintains a stable thermal environment, which in turn enables drift free signal evolution.

This performance enhancement is quantitatively captured in Fig. 1e[24,34,38,39,41-46] where the response time of the drift-free device outperforms conventional photodetectors by over three orders of magnitude, positioning our approach as a notable advancement in fast, stable FE optoelectronics.

Temporal and frequency-dependent photoresponse characteristics

When subject to pulsed illumination, the conventional BFO device exhibits a pronounced photocurrent drift, increasing from 39.13 to 121.04 μA during the illumination window (Fig. 2a); this represents a more than 200% increase in amplitude. This progressive rise reflects thermally activated charge accumulation, which produces artificial gain and delays carrier extraction[36]. A magnified view of the rising edge reveals a sluggish response time of 1648 ms is shown in Supplementary Fig. 1a. These characteristics underscore the intrinsic bottlenecks in low-thermal-conductivity-supported FE photodetectors. In contrast, the Cu-backed device maintains a stable, drift-free photocurrent profile when subject to identical illumination conditions (Fig. 2d). The negligible difference between the initial and peak photocurrent values confirms the effective suppression of thermal buildup. A magnified view of the rising edge (Supplementary Fig. 1b) reveals a fast temporal response of 1.7 ms, which is nearly 1000 times faster than the conventional device, hereby validating the role of controlled thermal pathways in accelerating photocarrier dynamics.

The influence of illumination power density on response time is further elucidating the thermal management role. For both architectures the response time decreases with increasing power density (Fig. 2b, 2e). However, the conventional device's response time (630 ms-1648 ms) is consistently three orders of magnitude slower than that of the drift-free device (0.8 ms-1.7 ms) across the measured illumination power density range. This vast difference underscores that the drift-free architecture, by providing a low thermal-resistance pathway, recovers the intrinsic electronic response time of the BFO layer. Recovery time trends (Supplementary Fig. 2) further confirm that it remains nearly illumination power-independent for both devices, with only a negligible increase at higher power densities. The millisecond-scale response time of the drift-free device is further substantiated by our frequency-domain analysis, where the extracted -3dB bandwidth and corresponding phase lag fall with in the 3-5 kHz range (Supplementary Note 1 and Supplementary Fig. 3). Consistent with this bandwidth, a direct time-domain measurement at 100 Hz modulation yields a stable undistorted waveform and a response time of 0.25 ms (Supplementary Fig. 4), confirming operation in the kilohertz regime.

The gain behavior at low-frequencies (50 mHz - 10 Hz), further highlights crucial role of thermal management. The conventional device suffers a ~20% gain roll-off below 5 Hz (Fig. 2c), indicative of the system's instability to reach the thermal equilibrium under modulated illumination. The drift-free device (Fig. 2f) demonstrates exceptional stability with a gain variation of $< 5\%$ across the same range. This flat frequency response is a direct consequence of the suppressed thermal time constant.

The gain power scaling of the two devices architectures (Fig. 2g, Supplementary Fig. 5, 6), measured over illumination power density range of 80 mW cm^{-2} to 2.5 mW cm^{-2}, reveals distinct thermal contributions to photocurrent generation. The conventional device exhibits a super-linear power-law dependance with a slope of 1.09, indicating that photocurrent increases faster than the incident photon flux. Such super-linearity is a well-known signature of thermally assisted carrier activation, where local temperature rise under continuous illumination enhances carrier population beyond direct photogeneration[37]. In contrast, the drift-free device shows a near-linear scaling with a slope of 0.92 indicating that the photocurrent is governed primarily by direct photocarrier generation and extraction. The suppression of super-linear gain reflects efficient vertical heat dissipation, which prevents thermal accumulation and minimizes temperature-induced carrier

amplification. This effective thermal management directly translates to improved figure of merits (FOM) for the drift-free device including lower noise current density, higher specific detectivity, and a superior signal to noise ratio (SNR), as detailed in the supporting information (Supplementary Note. 2 & Supplementary Fig. 7-12). The transition from super-linear to near-linear scaling thus provides direct evidence that thermal diffusion engineering effectively suppresses thermally driven gain enhancement and associated photocurrent drift[40].

To quantitatively validate the long-term stability of drift-free architecture, we performed systematic multi-hour and multi-day cycling experiments. Three independently fabricated devices were measured under identical modulated illumination (1Hz, 405 nm, 1.6 W cm^{-2}). Structural uniformity across these devices confirmed by SEM (Scanning electron microscopy) and AFM (Atomic force microscopy) (Supplementary Fig. 13, Fig. 14) shows consistent functional layers (BFO thickness: 66-73 nm; LNO thickness: 200-208 nm; RMS (root mean square) roughness: 1.09-1.24 nm) and lateral dimensions of 2 mm × 2 mm active area of all the devices. Each device exhibited the exceptional amplitude stability of 99.5-99.7% over continuous 2.7-hour segments (Supplementary Fig. 15). To prove extended duration, one device was monitored for 41.6 hours in sequential segments, maintaining > 97% stability with no observable degradation in temporal waveform shape as shown in Fig. 2h. Furthermore, repeated measurements on different days confirmed robust reproducibility with stability consistently in the 99.3 to 99.5% range (Supplementary Fig. 16). This comprehensive dataset, supported by uniform structural parameters.

Fig. 2i provides a comparative assessment of response times across a diverse set of FE photodetector systems, including BFO, lead titanate ($PbTiO_3$, PTO), lead zirconate titanate ($PbZr_{0.7}Ti_{0.3}O_3$, PZT), LNO, lead strontium tantalate ($Pb^{0.8}Sr_{0.2}TaO_3$, PST), barium calcium titanate ($Ba_{0.85}Ca_{0.15}TiO_3$, BCT), barium zirconium titanate ($BaZr_{0.1}Ti_{0.9}O_3$, BZT), barium calcium zirconium titanate ($Ba_{0.85}Ca_{0.15}Zr_{0.1}Ti_{0.9}O_3$, BCZT), barium titanate ($BaTiO_3$, BTO), and barium strontium zirconium titanate ($Ba_{0.8}Sr_{0.2}Zr_{0.1}Ti_{0.9}O_3$, BSZT), revealing a consistent performance enhancement in thermally engineered drift-free architectures (Supplementary Fig. 17, 18). All devices were fabricated and characterized in our laboratory under identical experimental conditions, using the same deposition method, electrode configuration, and a fixed active area of 2 mm × 2 mm, ensuring a fair and direct comparison across different material systems. Across all material platforms, drift-free devices exhibit accelerated temporal responses relative to their

conventional counterparts, frequently exceeding improvements of one to two orders of magnitude. This consistent behavior underscores the thermal diffusion engineering as an effective and broadly applicable strategy for enabling fast photodetection in a wide spectrum of FE materials. This performance is against state-of-the-art ferroelectric photovoltaic (FE-PV) and pyro-phototronic photodetectors, with the results compiled in Supplementary Table 1, confirming the competitive advantage of drift-free architecture.

Thermal engineering for drift suppression

To definitively attribute the observed drift-suppression to thermal management rather than other artifacts, we conducted dark-state control experiments under controlled temperature conditions. First, dark thermal-pulse measurement shows no pyroelectric current in either the conventional or drift-free architecture (Supplementary Note. 3 and Supplementary Fig. 19). Second, temperature-dependent dark I-V characteristics are identical for both devices conventional and drift-free (Supplementary Note. 4 and Supplementary Fig. 20, 21), proving the Cu backer solely modifies the thermal boundary condition without affecting interfacial chemistry or intrinsic charge transport.

To comprehensively evaluate and quantify the photocurrent instability in FE photodetectors, we introduce the parameters of *drift ratio* and *drift rate* (Fig. 3a). The drift ratio $\Delta I/I_1$ quantifies the relative change in photocurrent from its initial (I_1) to the peak (I_2), capturing the extent of the time-dependent photocurrent, while the drift rate $d(I/I_1)/dt$ reflects the temporal gradients of this change. These metrics provide a robust framework for comparing photocurrent stability across devices with varying substrate properties and thermal configurations. A comparative analysis of drift ratio across devices supported on freestanding, thermoplastic, and metallic substrates reveals a striking contrast (Fig. 3b). Devices on thermoplastics and freestanding mica exhibit a substantial drift ratio (>150%), consistent with inefficient heat dissipation (see Supplementary Fig. 22). In contrast, devices integrated with metallic substrates exhibit near-complete suppression of drift ratio (<5%), highlighting the important influence of a high substrate thermal conductivity in stabilizing the FE photoresponse when illuminated. This trend is further reinforced, by examining the drift rate as a function of illumination time window (Fig. 3c) which reflects how quickly thermally induced photocurrent changes develop. The freestanding and thermoplastic-supported devices exhibit high drift rates, particularly at short illumination times, which gradually stabilize at longer durations

(Supplementary Fig. 23-26). In contrast, the thermally conductive metallic substrates maintain consistently minimal drift rates across all time intervals, confirming effective suppression of thermal drift suppression (Supplementary Fig. 27-29). Optical absorption measurements confirm that the drift suppression is purely thermal, as all metallic backers (Cu. Al, SS) exhibit nearly identical absorption to the freestanding device; consistent with its minimal transmittance (0.6-1.7%), ruling out significant optical interference effects (Supplementary Note. 5 and Supplementary Fig. 30).

To establish a materials-level understanding of this behavior, we correlated the device drift characteristics with the intrinsic thermal conductivity of the supporting substrates (Fig. 3d). Thermoplastics exhibit thermal conductivities below 0.2 W m^{-1} K^{-1}, in contrast to metals, which exceed 100 W m^{-1} K^{-1}. This four-orders-of-magnitude disparity directly maps onto device performance. Experimental surface temperature measurements of each device subjected to 405 nm illumination (Fig. 3e) confirm this correlation (Supplementary Fig. 31). The conventional device without a heat sink reaches a temperature as high as 63 °C ($\Delta T \approx 38$ °C above room temperature), indicating heat accumulation, whereas the copper-supported device remains closer to ambient ($\Delta T \approx 6$ °C), signifying efficient vertical heat dissipation and reduced lateral spreading.

Infrared thermal imaging (Fig. 3f) of the devices visually confirms these trends. The conventional device exhibits isotropic lateral heat diffusion, forming broad circular hotspots that are fully consistent with lateral thermal diffusion and accumulation. In contrast the drift-free device backed with a copper substrate confines heat sharply at the illumination point, suppressing lateral thermal diffusion.

To theoretically validate these findings, we conducted computational simulations using the COMSOL Multiphysics software platform, specifically employing the Heat Transfer in Solids module (Fig. 3g). Time-dependent simulations using Fourier's law capture heat transport in both freestanding and copper-integrated architectures. In the conventional stack, heat diffuses radially with increasing time, closely matching the experimental IR thermography data (Supplementary Fig. 32). In contrast, a copper-backed structure sustains a confined vertical heat plume with negligible lateral spread. Detailed COMSOL Multiphysics simulations, presented in Supplementary Note. 6 and and Supplementary Videos 1,2, provide a comprehensive comparison of thermal behavior between the drift-free and conventional devices when subject to identical

illumination conditions. The simulations (Supplementary Video 1) reveal that the conventional device undergoes a substantial temperature rise (63 °C) and exhibits thermal non-uniformity across the device area. In contrast, the drift-free device shows markedly lower temperature increase (32 °C) even at higher intensities and maintains uniform thermal distribution across its structure. Furthermore, Supplementary video 2 highlights that conventional device reaches the same temperature differential at much lower light intensities (0.9 W cm^{-2}) compared to the drift-free device intensity (4.94 W cm^{-2}), underscoring the superior thermal regulation enabled by the high thermal conductivity and diffusivity of the Cu substrate. These findings confirm the critical role of vertical heat extraction in suppressing local thermal accumulation and stabilizing device operation under continuous optical excitation.

Extending our analysis across a broad spectrum of thermally engineered FE materials (BFO, PTO, PZT, LNO, PST, BCT, BZT, BCZT, BTO, BSZT), we observe a consistent reduction in both drift ratio and drift rate compared to their conventional counterparts (Fig. 3h and Supplementary Fig. 17). These results highlight the general applicability of thermal diffusion engineering strategy, which effectively enhances temporal stability and suppress thermally induced instabilities across diverse FE system.

Self-powered high-fidelity spatial imaging

High-fidelity spatial imaging is critical in modern electronic and optoelectronic systems, where precise detection, spatial localization of optical signals, and accurate mapping are essential for applications such as imaging sensors, optical communication, neuromorphic computing, and machine vision4[40,46]. However, achieving accurate spatial resolution in self-powered photodetectors is often hindered by lateral thermal diffusion, which introduces crosstalk between adjacent pixels or channels, distorting signal integrity. Here we demonstrate a schematic of the mode of device operation under selective illumination using a spatial mask, see Fig. 4a. Only a single channel of the device is exposed to light, while the neighboring channels are covered. In the conventional device, lateral thermal diffusion from the illuminated region results in spurious thermally induced voltage signals in the masked channels, thereby reducing spatial selectivity. In contrast, the drift-free device, which incorporates a thermally conductive copper substrate beneath the active layers, effectively limits lateral heat spread within the illuminated region. This thermal

confinement prevents heat spread into adjacent areas, resulting in a clean, isolated voltage signal only from the exposed channel-highlighting the device's superior spatial fidelity.

We also illustrate a conceptual design for a self-powered photodetector array used in imaging (Fig. 4b). A patterned light mask is projected onto the device, and the output voltage map is expected to reproduce the pattern with high accuracy. The experimental results using LabVIEW-based signal acquisition for photodetector arrays illuminated through "X" and "Z" shaped masks subjected to 405 nm light are provided (Fig. 4c). In the conventional devices, lateral heat conduction leads to detectable signals in the masked regions, blurring the spatial pattern. In contrast, the drift-free devices produce output signals that precisely match the illuminated shapes, confirming the suppression of thermal crosstalk and the ability to maintain sharp spatial boundaries between active and inactive regions. This superior spatial fidelity is quantitatively validated by a comprehensive analysis of channel crosstalk and the line-spread function (LSF), which show a seven-fold improvement in spatial confinement for the drift-free architecture (Supplementary Note. 7 and Supplementary Fig. 33-35). These findings establish the drift-free-FE photodetectors as a strong candidate for integration into spatially resolved optoelectronic systems, in particular where lower power consumption, fast response, and signal integrity are important. Further optimization, including systematic miniaturization to define the fundamental pixel-size-limits of this thermal-management strategy, presents a clear pathway for future high resolution imaging applications.

Discussion

We have demonstrated a thermal diffusion engineering strategy that addresses key limitations of ferroelectric photodetectors, enabling drift-free operation with fast temporal response times. By integrating a $BiFeO_3$ thin films onto high-thermal conductivity copper substrates, we achieve directional heat extraction that suppresses lateral thermal gradients, stabilizes local thermal environment. This leads to enhanced photoresponse speed and complete suppression of photocurrent drift. Frequency-domain measurements show a -3 dB bandwidth in the kHz regime consistent with the microsecond response scale device dynamics. Infrared thermal imaging and COMSOL Multiphysics simulations confirm that vertical heat confinement effectively eliminates lateral thermal diffusion. Spatially resolved measurement shows a seven-fold improvement in the line-spread function (LSF) and complete suppression of inter-channel cross talk, enabling high-

fidelity spatial imaging capability. Together with demonstrated long term operational stability, these results establish heat-flow as a key design parameter in FE optoelectronics, offering a scalable, material-agnostic approach for developing reliable, bias-free photodetectors suitable for neuromorphic vision, wearable sensing, and next-generation imaging systems.

Methods

Fabrication of $LaNiO_3$ (LNO) bottom electrode. The LNO precursor solution was synthesized via sol-gel route. $Ni(CH_3COO)_2 \cdot 4H_2O$ (nickel acetate-tetrahydrate) and $La(NO_3)_3 \cdot 6H_2O$ (lanthanum nitrate-hexahydrate) were dissolved into a mixture of anhydrous ethanol and glacial acetic acid (molar ratio 1:1) under steady magnetic stirring at room temperature until a homogeneous light-green solution was obtained. The solution (LNO) was spin-coated onto freshly cleaved muscovite mica substrate (2000 rpm, 30 s) using a programmable spin coater. Each deposited film was sequentially annealed at 200, 400, and 680 °C (3 min each) to remove organic residuals and crystallize the perovskite phase. This spin-coating and annealing cycle was repeated six times to achieve an LNO film with optimal conductivity and surface roughness.

Deposition of $BiFeO_3$ (BFO) and other FE layers. A stoichiometric BFO precursor solution (0.2 mol L^{-1}) was prepared by dissolving $Bi(NO_3)_3 \cdot 5H_2O$ (bismuth nitrate pentahydrate) and $Fe(NO_3)_3 \cdot 9H_2O$ (ferric nitrate nonahydrate) in ethylene glycol under ambient conditions. The solution (BFO) was spin-coated atop the LNO stack (4000 rpm, 30 s), followed by stepwise pyrolysis at 180, 350, and 550 °C (3 min each) to ensure gradual organic removal and crystallization. The deposition cycle yielded a BFO film with uniform morphology. The methodologies for depositing other FE materials including PTO, LNO, PZT, PST, BCT, BZT, BCZT, BTO, and BSZT follow analogous spin-coating methods.

Integration of ITO (top electrode) and conventional device assembly. An array of 2 mm × 2mm electrodes was patterned on the BFO surface using a shadow mask. The indium tin oxide (ITO) top electrode was deposited via RF magnetron (ZDF-5227 Composite Vacuum Gauge) sputtering (150 W, Ar Atmosphere, base pressure 4.5×10^{-6} Torr, 1200 s deposition time). Ohmic contacts were made by attaching copper wires to the ITO (top) and LNO (bottom) electrodes with conductive silver paste.

Drift-free device configuration. Freestanding devices were stacked onto different metallic and thermoplastic plates using a small amount of silver paste applied exclusively at the peripheral edges, ensuring no contact with electrodes or obstruction of the central active optical path. We prepared the other FE devices by following the same steps.

Device characterization and measurements.

Photoresponse measurements were performed using a combination of a Keithley 6514 electrometer and Keithley 2611B source-meter for low-noise current detection and electrical characterization. For time resolved measurements, the photocurrent signal was amplified using a low-noise current amplifier (Stanford Research system SR570) with suitable sensitivity with respect to the intensity of light and recorded with a mixed-domain oscilloscope (Tektronix MDO 3024). A low distortion function generator (Stanford Research system DS360) was used to modulate the laser intensity for frequency-dependent and transient response measurements. Calibrated laser source (MLL-III, DE52509) with wavelength 405 nm and power density of 320 mW cm^{-2} to 2.5 W cm^{-2} were employed, with the optical power monitored using a calibrated power meter (OPHIR PD300) (Supplementary Fig. 36).

For full frequency-response characterization, including gain and phase (Bode plots), a lock-in-amplifier (Stanford Research system SR865A) was employed.

Reflectance and transmittance spectra were measured using the OceanView Spectrophotometer equipped with a fiber-optic probe for the collection of reflected and transmitted light intensities, and the transmittance was further independently verified by using a UV-Vis spectrophotometer (Ultra 6600A).

For quantitative spatial metrics, including line-spread function (LSF) and crosstalk measurements, a microscope equid with a camera (TD-4KE) was used to focus the optical spot onto the device channel, while the sample was mounted on an x-y translational stage with micrometer-scale positioning accuracy to enable controlled scanning across the channel.

Temperature dependent I-V and transient measurements were carried out using a heating stage for temperature control, a Keithley 2260B source meter for voltage sourcing and a kiethely 6514 electrometer for high-sensitivity transient current recording.

Thermal Imaging: Transient temperature gradients during device operations were mapped using an Optris Xi 400 infrared thermal imager for both conventional and drift-free (with metallic substrate) devices.

Data acquisition: Voltage outputs were logged at the NI PXIe-1082 system with LabVIEW-based signal processing software. The measurements were conducted under the controlled illumination from a 405 nm light source, with optical patterning applied using two distinct mask shapes (Z and X). Data were collected for both conventional and drift-free device configurations to enable comparative analysis. All experimental parameters, including light intensity, sampling rate, and ambient conditions, were held constant across trials to ensure reproducibility.

Thermal Conductivity: Cross-plane thermal conductivity of individual layers was measured using a steady-state HS-DR-5 analyzer (error margin ± 5%).

Simulations: To theoretically validate our experimental observations, we performed comprehensive 3D thermal simulations using COMSOL Multiphysics (v6.1) with the "Heat transfer in solids" physics interface. The simulations were designed to replicate the exact geometric and material conditions of both conventional and drift-free-FE photodetectors, enabling direct comparison with experimental thermal imaging data (Fig. 3f-g).

Data availability

The data that supports the plots within this paper and other findings of the study are provided in supplementary information.

References

1. Dai, Y. et al. Self-Powered Si/CdS flexible photodetector with broadband response from 325 to 1550 nm based on pyro-phototronic effect: an approach for photosensing below bandgap energy. *Adv. Mater.* **30**, 1705893 (2018).
2. Zhou, Y. et al. Self-powered perovskite photon-counting detectors. *Nature* **616**, 712-718 (2023).
3. Han, S. et al. Tailoring of a visible-light-absorbing biaxial ferroelectric towards broadband self-driven photodetection. *Nat. Commun.* **12**, 284 (2021).

4. Wang, H. et al. A Self-powered, shapeable, and wearable sensor for effective hazard prevention and biomechanical monitoring. *SmartSys* **1**. e3 (2025).
5. Dong, F. et al. Skin-integrated wearable electronics: A dual-interface perspective. *SmartSys* **1**, e70013 (2025).
6. Martin, L. W. et al. Thin-film ferroelectric materials and their applications. *Nat. Rev. Mater.* **2**, 16087 (2017).
7. Wang, X. et al. Ultrasensitive and broadband MoS_2 photodetector driven by ferroelectrics. *Adv. Mater.* **27**, 6575-6581 (2015).
8. Wu, S. et al. Ultra-sensitive polarization-resolved black phosphorus homojunction photodetector defined by ferroelectric domains. *Nat. Commun.* **13**, 3198 (2022).
9. Yoshioka, K. et al. Ultrafast intrinsic optical-to-electrical conversion dynamics in a graphene photodetector. *Nat. Photonics* **16**, 718-723 (2022).
10. Liu, Y. et al. Ultrafast and ultra-broadband ferroelectric photo-pyroelectric detectors with long-term stability. *Adv. Funct. Mater.* **35**, 2502467 (2025).
11. Hu, C. et al. Quantifying the pyroelectric and photovoltaic coupling series of ferroelectric films. *Nat. Commun.* **16**, 828 (2025).
12. Yang, S. Y. et al. Above-bandgap voltages from ferroelectric photovoltaic devices. *Nat. Nanotechnol.* **5**, 143-147 (2010).
13. Yang, X. et al. Enhancement of photocurrent in ferroelectric films via the incorporation of narrow bandgap nanoparticles. *Adv. Mater.* **24**, 1202-1208 (2012).
14. Rubio-Marcos, F. et al. Reversible optical control of macroscopic polarization in ferroelectrics. *Nat. Photon.* **12**, 29-32 (2018).
15. Choi, T. et al. Switchable ferroelectric diode and photovoltaic effect in $BiFeO_3$. Science **324**, 63-66 (2009).
16. Yi, H. T. et al. Mechanism of the switchable photovoltaic effect in ferroelectric $BiFeO_3$. *Adv. Mater.* **23**, 3403-3407 (2011).
17. Nechache, R. et al. Bandgap tuning of multiferroic oxide solar cells. *Nat. Photon.* **9**, 61-67 (2014).
18. Li, Z. et al. Self-powered visible light photodetector based on Bi_xFeO_3 film. *Ceram. Int.* **48**, 2811-2819 (2022).

19. Xing, J. et al. High-sensitive switchable photodetector based on $BiFeO_3$ film with in-plane polarization. *Appl. Phys. Lett.* **106**, 033504 (2015).
20. Dho, J. et al. Large electric polarization and exchange bias in multiferroic $BiFeO_3$. *Adv. Mater.* **18**, 1445-1448 (2006).
21. Liou, Y. D. et al. Deterministic optical control of room temperature multiferroicity in $BiFeO_3$ thin films. *Nat. Mater.* **18**, 580-587 (2019).
22. Long, L. et al. Regulation of multiferroicity in $BiFe_{1-x}Cr_xO_3$ thin films fabricated employing sol-gel process. *J. Mater. Sci.: Mater. Electron.* **33,** 11308-11317 (2022).
23. Rovillain, P. et al. Electric-field control of spin waves at room temperature in multiferroic $BiFeO_3$. *Nat. Mater.* **9**, 975-979 (2010).
24. Kathirvel, A. et al. $BiFeO_3$-thiourea/carbon heterostructure based self-powered white light photodetector. *Mater. Lett.* **284**, 128906 (2021).
25. Xu, A. et al. Enhanced photoelectric and thermoelectric coupling factor in $BiMn_2O_5$ ferroelectric film. Adv. Powder Mater. **4**, 100260 (2025).
26. Wu, Bo, et al. Indirect tail states formation by thermal-induced polar fluctuations in halide perovskites. *Nat. Commun.* **10**, 484 (2019).
27. Bansal, S. et al. Design and TCAD analysis of few-layer graphene/ZnO nanowires heterojunction-based photodetector in UV spectral region. *Sci. Rep.* **15**, 17762 (2025).
28. Mahapatra, A. et al. Understanding the origin of light intensity and temperature dependence of photodetection properties in a $MAPbBr_3$ single-crystal-based photoconductor. *ACS Photonics.* **10**, 1424-1433 (2023).
29. Kim, Y. M. et al. Direct observation of ferroelectric field effect and vacancy-controlled screening at the $BiFeO_3/La_xSr_{1-x}MnO_3$ interface. *Nat. Mater.* **13**, 1019-1025 (2014).
30. Le, H. K. et al. Room-temperature ferroelectric epitaxial nanowire arrays with photoluminescence. *Nano Lett.* **24**, 5189-5196 (2024).
31. Ma, C. H. et al. Van der Waals epitaxy of functional MoO_2 film on mica for flexible electronics. *Appl. Phys. Lett.* **25**, 108 (2016).
32. Whatmore, R. W. Pyroelectric devices and materials. *Rep. Prog. Phys.* **49**, 1335-1386 (1986).
33. You, L. et al. Enhancing ferroelectric photovoltaic effect by polar order engineering. *Sci. Adv.* **4**, eaat3438 (2018).

34. Qi, J. et al. Enhanced photocurrent in $BiFeO_3$ materials by coupling temperature and thermo-phototronic effects for self-powered ultraviolet photodetector system. *ACS Appl. Mater. Interfaces* **10**, 13712-13719 (2018).
35. Viana, E. R. et al. Photoluminescence and high-temperature persistent photoconductivity experiments in SnO_2 nanobelts. *J. Phys. Chem.* C **117,** 7844-7849 (2013).
36. Jia, C. et al. Ferroelectrically modulated and enhanced photoresponse in a self-powered α-In2Se3/Si heterojunction photodetector. *ACS Nano* **17**, 6534-6544 (2023).
37. Stewart, J. W. et al. Nanophotonic engineering: A new paradigm for spectrally sensitive thermal photodetectors. *ACS Photonics* **8.** 71-84 (2020).
38. Ma, S. et al. Boosting the photoresponse speed of visible-light-active bismuth ferrite thin films based on Fe-site substitution strategy and favorable heterostructure design. *Appl. Surf. Sci.* **590**, 153054 (2022).
39. Yang, L. et al. Boosted photocurrent via heating $BiFeO_3$ thin film for UV photodetector at wide temperature range. *Adv. Funct. Mater.* **33**, 2303408 (2023).
40. Qi, J. et al. Photovoltaic-pyroelectric coupled effect based nanogenerators for self-powered photodetector system. *Adv. Mater. Interfaces* **5,** 1701189 (2018).
41. Lam, S. M. et al. A newly emerging visible light-responsive $BiFeO_3$ perovskite for photocatalytic applications: a mini review. *Mater. Res. Bull.* **90**, 15-30 (2017).
42. Mondal, S. et al. Efficient flexible white-light photodetectors based on $BiFeO_3$ nanoparticles. *ACS Appl. Nano Mater.* **1**, 625-631 (2018).
43. Upadhyay, R. K. et al. Solid-state synthesized $BiFeO_3$ perovskite-based fast-response white-light photodetector. *IEEE Electron Device Lett.* **41**, 1225-1228 (2020).
44. Biswas, P. P. et al. Polarization driven self-biased and enhanced UV-visible photodetector characteristics of ferroelectric thin film *J. Phys. D: Appl. Phys.* **53,** 275302 (2020).
45. Wang, J. et al. Ferroelectric photodetector with high current on-off ratio (∼1 × 104%) in self-assembled topological nanoislands. *ACS Appl. Electron. Mater.* **1**, 862-868 (2019).
46. Ma, G. et al. A broadband UV-visible photodetector based on a Ga_2O_3/BFO heterojunction. *Phys. Scr.* **96**, 125823 (2021).

Acknowledgements

This work was supported by the Beijing Natural Science Foundation (Grant No. 2244109), the National Natural Science Foundation of China (Grant No. 52072041), the Beijing Natural Science

Foundation (Grant No. JQ21007), the University of Chinese Academy of Sciences (Grant No. Y8540XX2D2), and the ANSO (Alliance of International Science Organizations).

Author contributions

Y.Y. conceived the idea and supervised the project. J.Z.M. and C.G. synthesized the composite materials. J.Z.M., W.Q., and L.X. carried out the device fabrication and electrical measurements. J.Z.M. carried out the theoretical simulations. J.Z.M., W.Q., L.X., C.G. and Y. Y. analyzed the experimental data. J.Z.M., L.X., C.R.B. and Y. Y. co-wrote the manuscript. All the authors discussed the results and commented on the manuscript.

Competing Interests

The authors declare no competing interests.

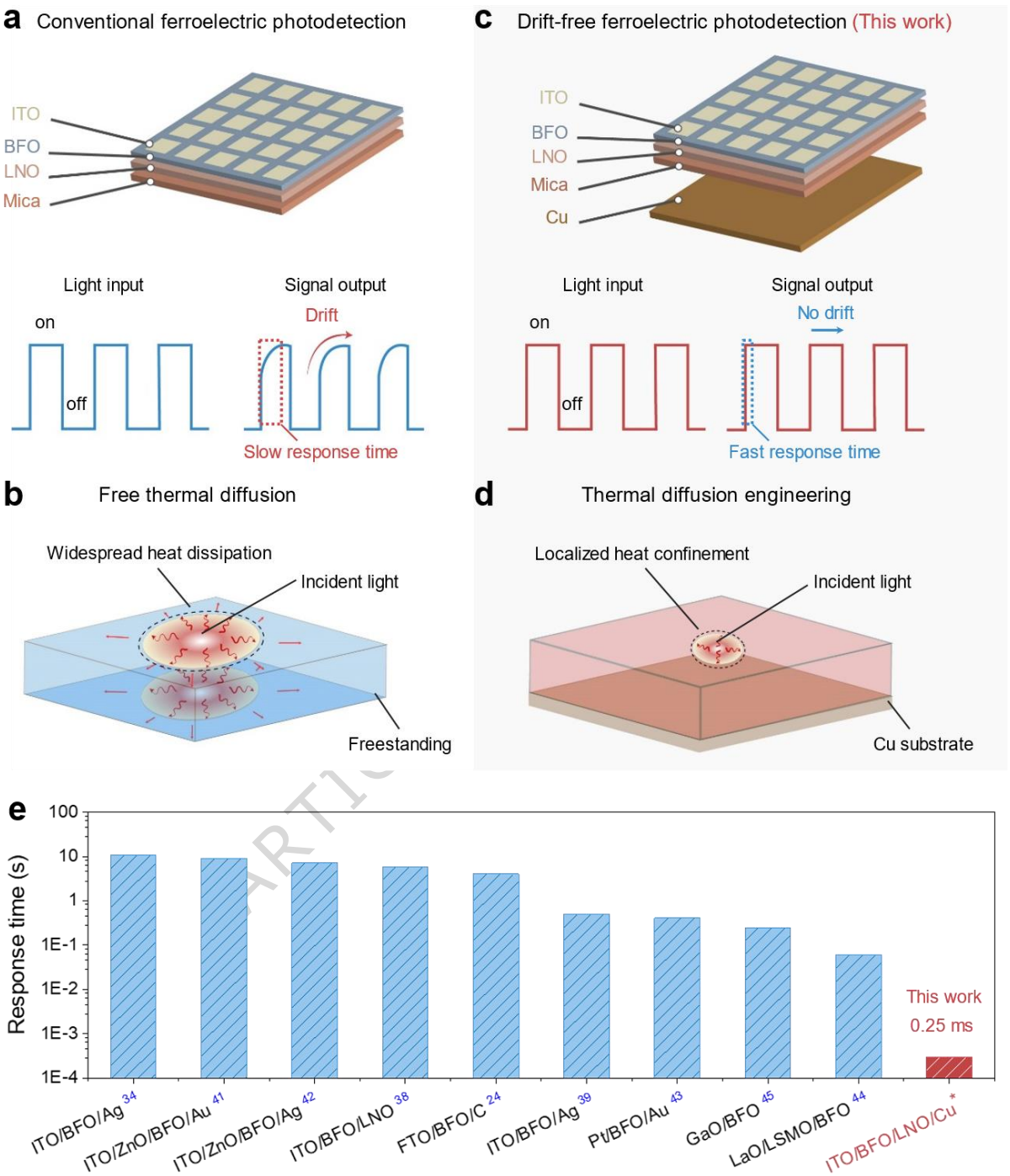

Fig. 1 | Schematic of conventional vs drift-free fast temporal photodetection via thermal diffusion engineering. a, Conventional ferroelectric device (LNO/BFO/ITO on a mica substrate) in freestanding condition. Output signal (right) exhibits slow response time (dotted line) and photocurrent drift (curved arrow). **b,** Schematic of free thermal diffusion in conventional device. **c,** Drift-free photodetection with a copper substrate. Output signal (right) shows fast response time (dotted line) and no drift (straight arrow). **d,** Schematic of engineered thermal diffusion with

localized heat confinement due to copper substrate. **e,** Comparison of response time: our drift-free device (red bar) demonstrates fast performance compared to slow responses (blue bars) in prior work.

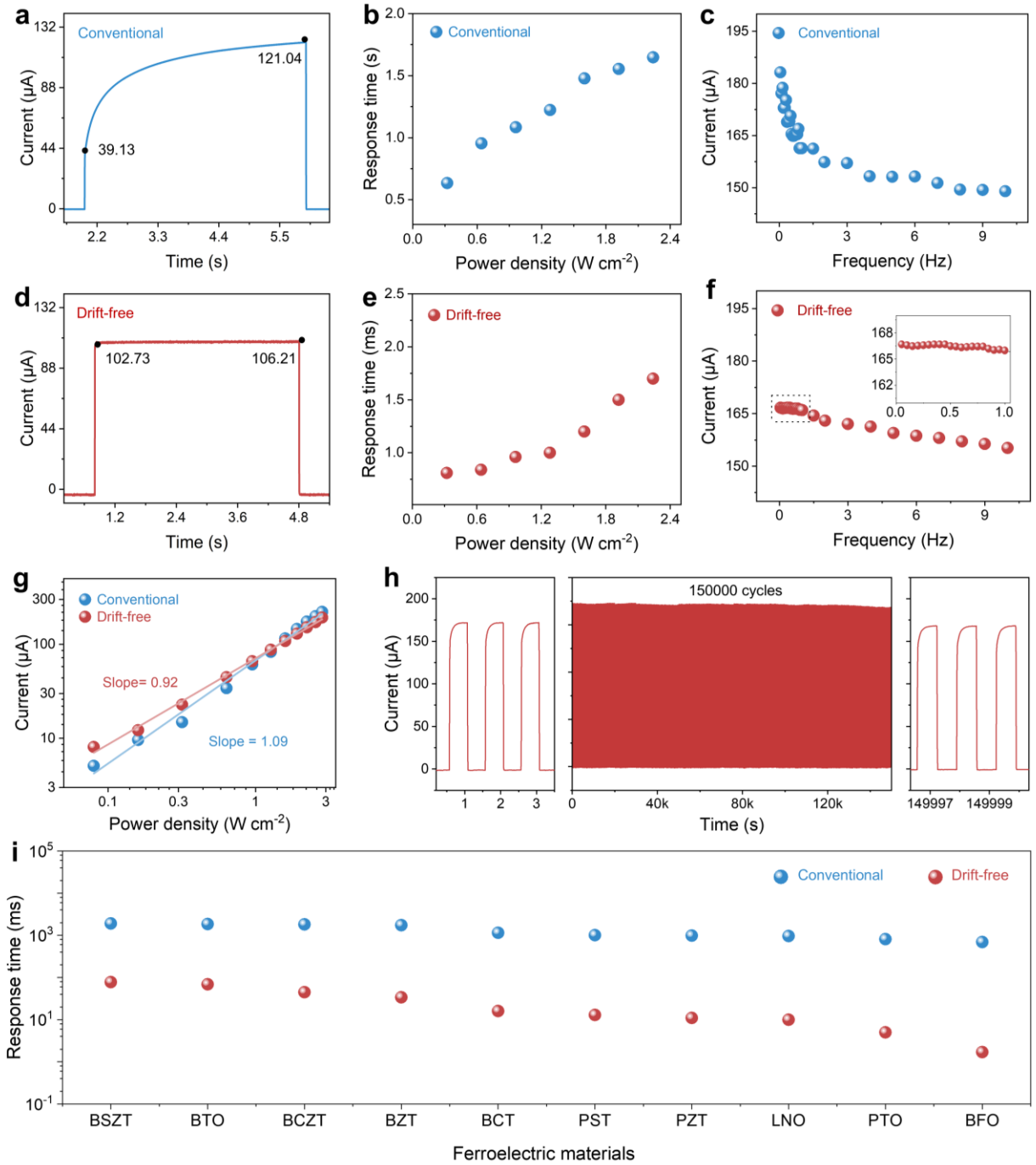

Fig. 2 | Quantitative comparison of conventional and drift-free photodetector architectures. **a,d,** Time-resolved photocurrent under constant illumination, showing pronounced photocurrent drift in the conventional device **(a)** and a stable steady-state response in the drift-free device **(d)**. **b,e** Illumination power density-dependent response times showing 3 orders of slower response for conventional **(b)** device (630 ms - 1648 ms) in comparison of drift-free **(e)** architectures response (0.8 ms-1.7 ms). **c,f,** Low-frequency photocurrent gain stability (50 mHz–10 Hz) for conventional (**c**) and drift-free (**f**) devices. **g,** Illumination power denisty-dependent gain scaling at high and low

illumination intensities. The conventional device (slope ≈1.08, super-linear region) and the drift-free device (slope ≈ 0.92) shows nearly linear scaling. **h**, Long-term operational stability of a drift-free device over a 41.6-hour (2.7-hours segmented) measurement under 1.6 W cm^{-2} illumination, exhibiting minimal amplitude drift of < 3%. **i,** Comparison of response time of different ferroelectric devices (conventional and drift-free) fabricated under the identical condition with same electrodes, and identical active area of 2 mm × 2 mm.

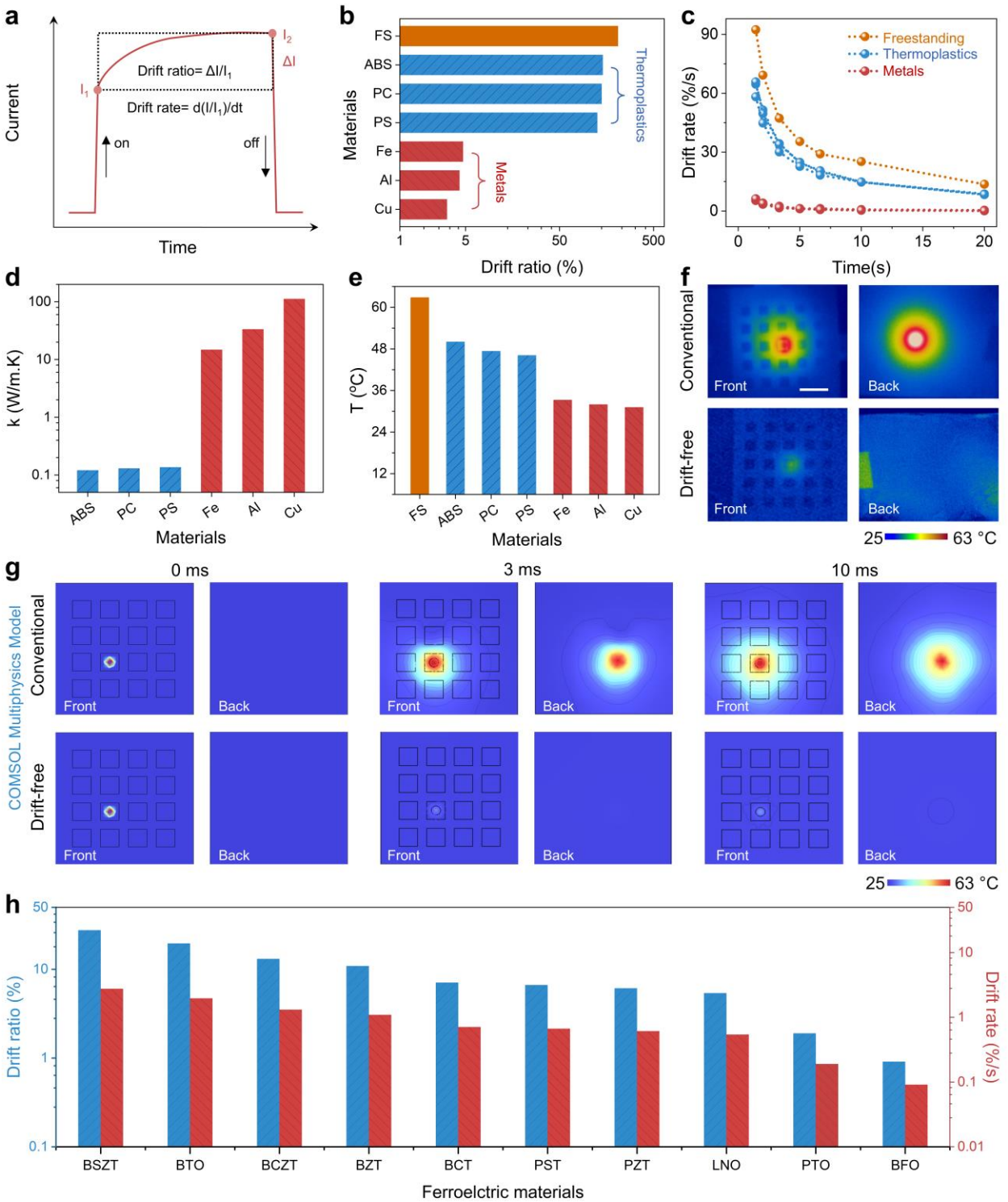

Fig. 3 | Thermal diffusion engineered drift suppression in ferroelectric photodetector. a, Definition of drift ratio and drift rate from photocurrent transients. **b-c,** Metallic substrate minimizes (**b**) drift ratio and (**c**) drift rate compared to thermoplastics and freestanding

configurations. Thermoplastics include acrylonitrile butadiene styrene (ABS), polycarbonate (PC), and polystyrene (PS), while metallic substrates include iron (Fe), aluminum (Al), and Cu (copper). **d,** Thermal conductivity (k) of tested substrate materials, showing that metals outperform polymers by two orders of magnitude**. e,** Temperature rises under illumination: conventional devices reach 63 °C (ΔT = 38 °C), while the copper-backed device stabilizes at 31 °C (ΔT = 6 °C). **f,** Infrared thermography confirms lateral heat spreading in conventional devices vs. confined heating in drift-free design. **g,** COMSOL simulations validate experimental trends, showing rapid heat diffusion in freestanding devices vs. heat confinement in metal-integrated devices. **h,** Generality of thermal diffusion engineering across diverse ferroelectric devices.

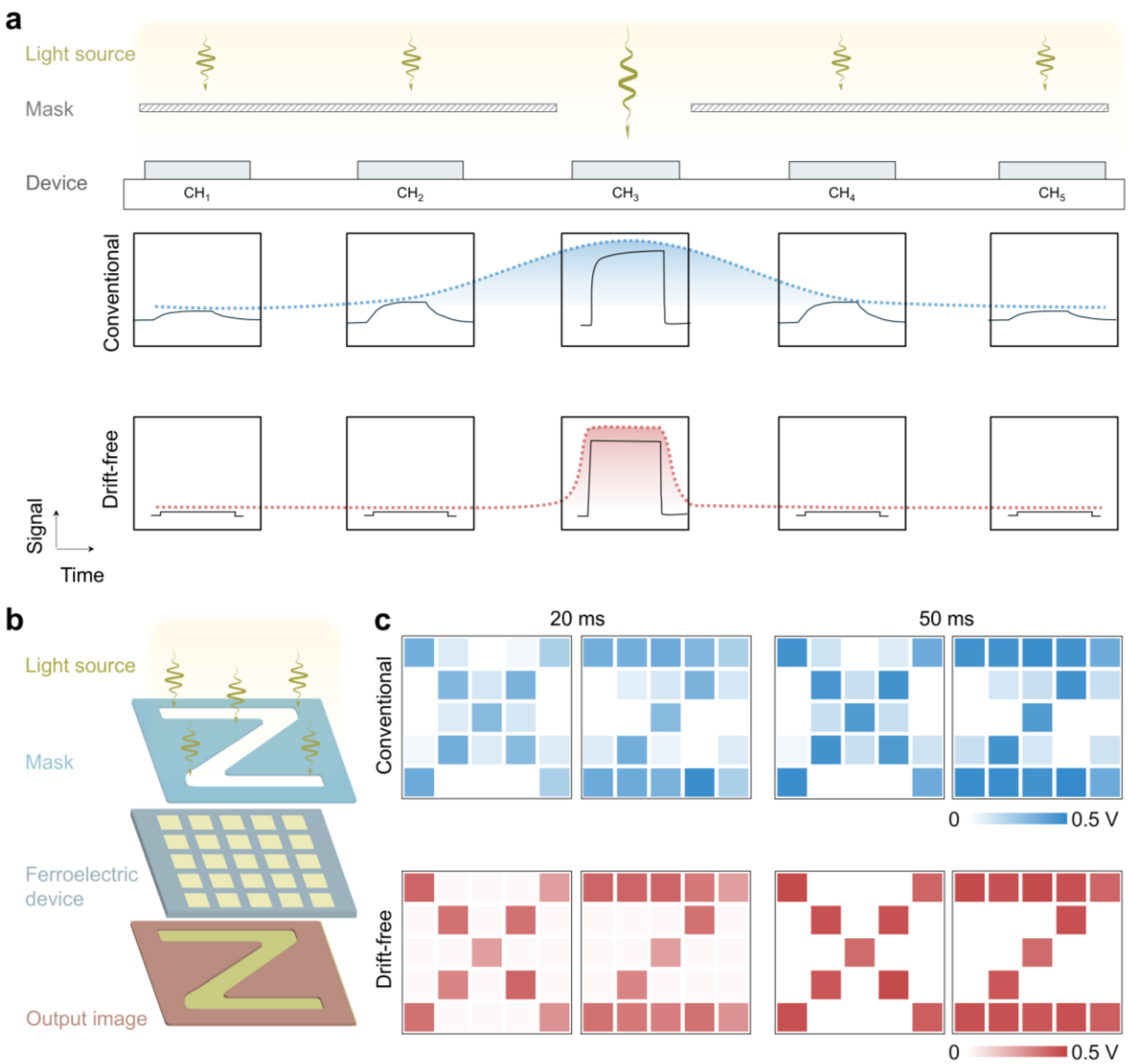

Fig. 4 | Self-powered high-fidelity spatial imaging enabled by thermal-diffusion engineering. **a,** Schematic of output signals under masked illumination: the conventional device shows false signals in covered channels due to lateral heat spread, while drift-free devices confine heat to the exposed channel, eliminating crosstalk. **b,** Proposed self-powered imaging array design, integrating a mask layer with drift-free ferroelectric pixels for spatially accurate detection. **c,** Experimental validation: X and Z shaped irradiations (405 nm) demonstrate that drift-free devices prevent thermal crosstalk into masked regions, unlike conventional detectors.

Editor's summary:

Thermal diffusion engineering enables drift-free ferroelectric photo detectors with fast temporal response by stabilizing heat flow. The approach overcomes long-standing limitations of ferroelectric devices and offers a scalable route to high-performance optoelectronics.

Peer review information: *Nature Communications* thanks Mohit Kumar, Thomas Pucher and the other anonymous reviewer(s) for their contribution to the peer review of this work. A peer review file is available.